electronics

MDPI

Article

Maneuvering Trajectory Synthetic Aperture Radar Processing Based on the Decomposition of Transfer Functions in the Frequency Domain Using Average Blurred Edge Width Assessment

Chenguang Yang [1], Duo Wang [1], Fukun Sun [2] and Kaizhi Wang [1,3,*]

[1] School of Electronic Information and Electrical Engineering, Shanghai Jiao Tong University, Shanghai 200240, China; wangduoup@sjtu.edu.cn (D.W.)
[2] Aerospace Information Research Institute, Chinese Academy of Sciences, Beijing 100190, China; sunfk@aircas.ac.cn
[3] Yiwu Zhiyuan Research Center of Electronic Technology, Yiwu 322000, China
* Correspondence: kz_wang@sjtu.edu.cn

Abstract: With the rapid development of synthetic aperture radar (SAR), delivery platforms are gradually becoming diversified and miniaturized. The SAR flight process is susceptible to external influences, resulting in unsatisfactory imaging results, so it is necessary to optimize imaging processing in combination with the SAR imaging quality assessment (IQA) index. Based on the principle of SAR imaging, this paper analyzes the impact of defocusing on imaging results caused by mismatched filters and draws on the assessment algorithm of motion blur, proposing a SAR IQA index based on average blurred edge width (ABEW) in the salient area. In addition, the idea of decomposing the transfer function in the frequency domain and fitting the matched filter with a polynomial is also proposed. The estimation of the flight trajectory is changed to a correction of the matched filter, avoiding the precise estimation of Doppler parameters and complex calculations during the time–frequency conversion process. The effectiveness of ABEW was verified by using SAR images of real scenes, and the results were highly consistent with the actual image quality. The imaging processing was tested using the echo signals generated by the errors introduced during the flight process, and more satisfactory imaging results were obtained by using ABEW with the filter for correction. The imaging process was tested using the echo signal generated by introducing errors during the flight, and the filter was corrected using ABEW as an index, obtaining a comparatively ideal imaging result.

Keywords: synthetic aperture radar; imaging processing; image quality assessment; matched filtering; defocus

check for updates

Citation: Yang, C.; Wang, D.; Sun, F.; Wang, K. Maneuvering Trajectory Synthetic Aperture Radar Processing Based on the Decomposition of Transfer Functions in the Frequency Domain Using Average Blurred Edge Width Assessment. *Electronics* **2024**, *13*, 4100. https://doi.org/10.3390/electronics13204100

Academic Editor: Massimiliano Pieraccini

Received: 19 August 2024
Revised: 13 October 2024
Accepted: 17 October 2024
Published: 17 October 2024

Copyright: © 2024 by the authors. Licensee MDPI, Basel, Switzerland. This article is an open access article distributed under the terms and conditions of the Creative Commons Attribution (CC BY) license (https://creativecommons.org/licenses/by/4.0/).

1. Introduction

Synthetic aperture radar (SAR) is widely used in military and civilian applications because it can be used at any time of the day under all weather conditions [1,2], and it can produce high-resolution outputs. In a variety of applications, SAR is expected to detect and recognize targets rapidly [3–5], and the quality of imaging results seriously affects the detection speed and recognition accuracy. With the rapid development of SAR, delivery platforms are gradually diversified and miniaturized. For example, flexible unmanned aerial vehicles (UAVs) are now used as radar carriers [6,7]. However, precisely because of the lightweight nature of UAVs, their flight processes are more susceptible to external influences, resulting in unstable flight trajectories. The deviation of the trajectory will cause serious defocusing in the azimuth [8,9]. Motion estimation and compensation are required, and the imaging results are evaluated using SAR image quality assessment (IQA) indexes.

Eldhuset analyzed the limitations of traditional models for SAR high-resolution imaging, provided a flight model for curved trajectory SAR [10,11], and proposed an imaging method using a fourth-order transfer function for matched filtering. This method uses Doppler parameters to fit the flight trajectory in the time domain and expresses the instantaneous distance as a fourth-order polynomial. The frequency domain expression of the echo signal is then obtained using the principle of stationary phase (POSP) twice [12], and the matched filter is generated based on this. Imaging processing is achieved by multiplying the matched filter with the echo data in the 2D frequency domain. Then, the accuracy of flight trajectory fitting is closely related to the accuracy of parameter estimation. In order to obtain flight parameters, researchers integrated a global positioning satellite (GPS) receiver and inertial measurement unit (IMU) onto the radar platform [13–15]. GPS provides the location information of the flight platform, and IMU provides the attitude information of the flight platform. The sensor information is recorded simultaneously with the radar raw data to perform correct image geocoding. However, with the improvement in SAR resolution, the accuracy of the sensor can no longer meet these needs. In addition, the vibration of the platform also degrades the quality of the measurements performed by the sensor. In order to solve the above problems, a variety of methods for estimating Doppler parameters from echo data have been proposed, such as the amplitude-based map drift method [16,17] and the phase-based phase gradient method [18,19]. However, these algorithms are complex and add extra calculations. In addition, in the process of using POSP to calculate the frequency domain expression, the instantaneous distance expressed by a high-order polynomial will introduce a high-order equation, which is computationally complex [20].

For most image systems, for the purpose of human visual perception, the subjective assessment method is the most accurate IQA method [21,22]. However, the subjective assessment method requires a large amount of manual intervention, which is time-consuming and laborious and can no longer handle the current flood of image information brought about by the development of networks. Therefore, defining an objective IQA index has become an important research direction in the field of image processing. Different from the passive imaging principle of optical images, SAR is an active remote sensing system working in the microwave band. Its imaging principle is fundamentally different from optical imaging. Taking into consideration the fact that SAR images are grayscale images that reflect the backscattering characteristics of targets and have strong texture characteristics, Jiao Shuhong et al. modified and improved the original structural similarity (SSIM) algorithm by introducing the texture information of SAR images and proposed a texture-based SSIM (TSSIM) algorithm suitable for SAR images [23]. However, the TSSIM algorithm requires the original image as a reference, and in many cases, such as in SAR imaging processing, there is no original optimal image for reference, so the usage situation will be limited. The traditional SAR non-reference IQA indexes are mainly proposed based on the statistical characteristics of point and area targets. Indexes such as peak sidelobe ratio, integrated sidelobe ratio, spatial resolution, and others are calculated using the impulse response function of point targets [24,25], while the mean, variance, information entropy, dynamic range, equivalent number of looks, and radiation resolution all reflect the characteristics of surface targets. However, these indexes are not combined with the principle of SAR imaging focusing, so there are often failures.

SAR imaging processing can be attributed to the process of precise matched filtering. A matched filter is used in the frequency domain to retain the position information of the target while canceling out the excess phase; it is then converted back to the time domain through time–frequency conversion, and all the energy is concentrated at the position corresponding to the target, thereby achieving SAR imaging. When the flight trajectory is not ideal, the defocus in the imaging result is actually due to a mismatch of the filter. The purpose of fitting the flight trajectory in the time domain is also to obtain a filter that matches the echo data. Therefore, based on the principle of SAR imaging, this paper analyzes the impact of defocusing caused by the mismatched filter on imaging results, and draws on the assessment algorithm of motion

blur to propose an SAR IQA index based on average blur edge width (ABWE) in the salient area. Compared with the traditional SAR IQA indexes, this index has higher accordance with the actual image quality, providing the new idea and method for the IQA of SAR. In addition, a method of decomposing the transfer function and fitting the matched filter with polynomials in the frequency domain instead of fitting the flight trajectory with polynomials in the time domain is also proposed. The estimation of the flight trajectory is converted into a correction of the matched filter, avoiding the precise estimation of Doppler parameters and complex calculations in the time–frequency conversion process. The matched filter is approximated by a fourth-order polynomial, and the physical meaning of each term and the degree of impact on the quality of the imaging results are analyzed. In order to verify the feasibility of this idea, errors are introduced during the flight to generate an echo signal for testing, and the filter is corrected in conjunction with ABEW. The experimental results show that, compared with the pre-correction, the corrected matched filter can be used to obtain more ideal imaging results, providing a new idea and method for echo data imaging processing when the flight trajectory is not ideal.

2. Principles and Methods

2.1. Two-Dimensional Matched Filtering

When the radar maintains an ideal side-looking working mode on the aircraft, the hyperbolic model distance equation from the radar to the target can be expressed as follows:

$$r(t) = \sqrt{R_0^2 + v^2 t^2} \tag{1}$$

where R_0 is the shortest slant range from the radar to the target, v is the velocity of the platform, and t is the azimuth time.

The typical SAR echo signal is represented as follows:

$$s_0(\tau, t) = A_0 w_r\left(\tau - \frac{2r(t)}{c}\right) w_a(t - t_c) exp\left\{j\pi k_r\left[\tau - \frac{2r(t)}{c}\right]^2 - j\frac{4\pi r(t)}{\lambda}\right\} \tag{2}$$

where j is the imaginary number unit, $j = \sqrt{(-1)}$; c is the speed of light; A_0 is a complex constant; τ is the range time; k_r is the range frequency modulation rate; λ is the wavelength corresponding to the carrier frequency; w_r is the pulse envelope, which can usually be approximated as a rectangle; w_a is the envelope of the azimuthal signal; and t_c is the moment when the beam center passes the target.

Range Fourier transform is performed on Equation (2), and the POSP is used to obtain the following:

$$S_0(f_\tau, t) = A_1 W_r(f_\tau) w_a(t - t_c) exp\left(-j\frac{\pi f_\tau^2}{k_r}\right) exp\left[-j\frac{4\pi(f_c + f_\tau) r(t)}{c}\right] \tag{3}$$

where A_1 is a constant introduced by A_0 and the range Fourier transform, f_c, is the carrier frequency, W_r is the spectral envelope in the range direction, and f_τ is the frequency in the range direction. Then, POSP is used in the azimuth direction of Equation (3) to obtain the signal spectrum as follows:

$$S_{2df}(f_\tau, f_a) = A_2 W_r(f_\tau) W_a(f_a - f_{ac}) exp\left\{j\theta_{2df}(f_\tau, f_a)\right\} \tag{4}$$

where A_2 is a constant introduced by A_1 and the azimuth Fourier transform, $W_a(f_a - f_{ac})$ is the azimuth spectrum envelope centered on the Doppler center frequency f_{ac}, and $\theta_{2df}(f_\tau, f_a)$ is the phase after Fourier transform, expressed as

$$\theta_{2df}(f_\tau, f_a) = -\frac{4\pi R_0 f_c}{c}\sqrt{D^2(f_a, v) + \frac{2f_\tau}{f_c} + \frac{f_\tau^2}{f_c^2}} - \frac{\pi f_\tau^2}{k_r} \tag{5}$$

in which

$$D(f_a, v) = \sqrt{1 - \frac{c^2 f_a^2}{4v^2 f_c^2}} \tag{6}$$

To analyze the physical meaning of Equation (5), we expand the square root in Equation (5) into a power series of f_τ and retain until the f_τ^2 term, $\theta_{2df}(f_\tau, f_a)$, becomes

$$\theta_{2df}(f_\tau, f_a) = -\frac{4\pi R_0 f_c}{c}\left[D(f_a, v) + \frac{f_\tau}{f_c D(f_a, v)} - \frac{f_\tau^2}{2f_c^2 D^3(f_a, v)}\frac{c^2 f_a^2}{4v^2 f_c^2}\right] - \frac{\pi f_\tau^2}{k_r} \tag{7}$$

where the first term in the brackets comes from the azimuth modulation, the second term comes from the range cell migration (RCM), and the last term comes from the cross-coupling between the range and the azimuth.

The design of the matched filter should be able to eliminate the redundant phase in Equation (5), so that the target appears at the corresponding position after matched filtering, and retain the phase introduced by the target range R_0 (for interference and polarization applications that require the actual phase of the target). Then, the phase of the matched filter will be

$$\theta_{MF}(f_\tau, f_a) = -\theta_{2df}(f_\tau, f_a) - \frac{4\pi R_0 f_c}{c} - \frac{4\pi R_0 f_\tau}{c} \tag{8}$$

in which the second term is the phase introduced by the target range R_0, and the third term represents the range position of the point target, where the target peak will appear after matched filtering.

The result of the matched filtering is

$$s_1(\tau, t) = A_3 p_r\left(\tau - \frac{2R_0}{c}\right) p_a(t - t_c) exp\left(-\frac{4\pi R_0 f_c}{c}\right) \tag{9}$$

where A_3 is a constant introduced by A_2 and the two-dimensional Fourier inverse transform, and p_r and p_a are the Fourier inverse transforms of the window function. For rectangular windows W_r and W_a and p_r and p_a are *sinc* functions. The envelope of Equation (9) shows that the target is located at $\tau = \frac{2R_0}{c}$, $t = t_c$ at this time.

Thus far, we have analyzed the fundamental principles of SAR imaging through matched filtering. Building on this foundation, we will further explore the effects of filter mismatch on imaging results and corrections to the filter in the frequency domain.

2.2. Mismatch of the Matched Filter

According to the principle of matched filtering, SAR focusing needs to accurately determine the distance between the scatterer and the sensor and correct the related phase delay. The generation of defocus is mainly due to the incorrect assumption that the antenna phase center passes through a path at a known velocity during imaging, when in fact the radar deviates from this path. Radar orbit deviation will cause an uncertain Doppler modulation of the received signal, resulting in the mismatch between the azimuth matched filter and the frequency modulation rate of the received signal. As a result, the SAR image is unable to be focused in the azimuth direction, and this is shown as the azimuth trailing blur, similar to the motion blur in the ordinary image.

Assuming that the pulse duration is T and the frequency modulation rate in the azimuth direction is K_a, the typical SAR echo signal in the azimuth direction is represented as follows:

$$s_a(t) = rect\left(\frac{t}{T}\right) \exp\left(j\pi K_a t^2\right) \tag{10}$$

The ideal azimuth matched filter is

$$h_a(t) = rect\left(\frac{t}{T}\right) \exp\left(-j\pi K_a t^2\right) \tag{11}$$

The result of matched filtering for Equations (10) and (11) is as follows:

$$\begin{aligned} s_{out}(t) &= s_a(t) \otimes h_a(t) \\ &= \exp\left(j\pi K_a t^2\right) \int_{-T/2}^{+T/2} \exp(-j2\pi K_a t u) du \\ &\approx T \sin c(K_a T t) \end{aligned} \tag{12}$$

in which the symbol $\int$ represents the integral, indicating the integration of the function $\exp(-j2\pi K_a t u)$ with respect to the variable u over the interval $[-T/2, +T/2]$.

When the azimuth matched filter is mismatched, Equation (11) changes to

$$h_{error} = rect\left(\frac{t}{T}\right) \exp\left\{-j\pi(K_a + \Delta K)t^2\right\} \tag{13}$$

where ΔK is the error of the azimuth frequency modulation rate. In this case, the result of matched filtering is

$$\begin{aligned} s_{error} &= s_a(t) \otimes h_{error}(t) \\ &= \int_{-T/2}^{+T/2} \exp\left(-j\pi \Delta K u^2\right) \exp(-j2\pi K_a t u) du \end{aligned} \tag{14}$$

According to Equations (12) and (14), it can be seen that when the error of frequency modulation rate is zero, the echo signal after matched filtering is a $\sin c$ function. When there is an error in the frequency modulation rate, the impulse response width will widen and the sidelobe will increase, as shown in Figure 1. According to Figure 1, it can be seen that despite a small degree of error, the degradation of the image quality is extremely serious. The effect of using a mismatched filter on imaging results in real-scene SAR echo imaging processing is shown in Figure 2. Figure 2a shows the result of matched filtering using an ideal filter, and Figure 2b shows the result when a mismatched filter is used. It can be seen in Figure 2b that a tailing phenomenon is produced in the azimuth.

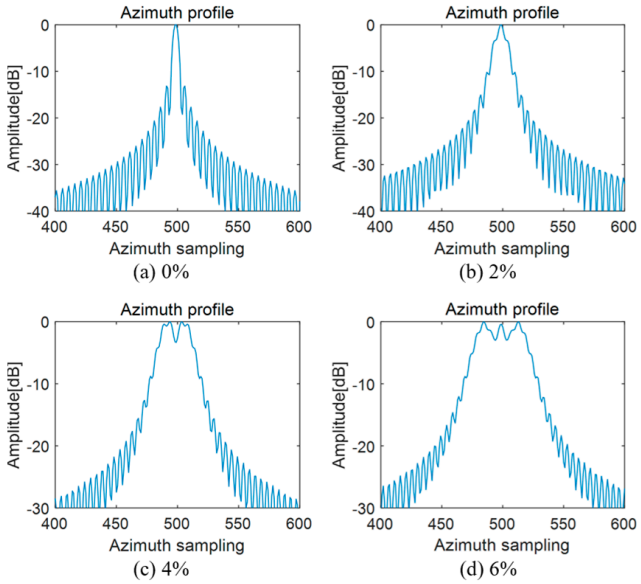
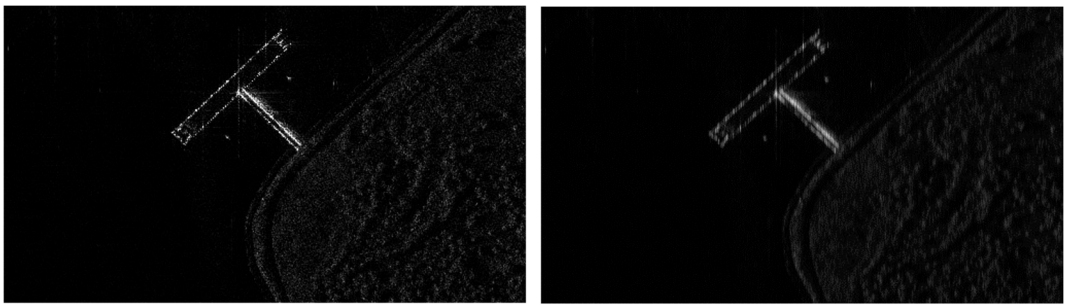


Figure 1. The impact of azimuth frequency modulation rate error on point targets. The percentages in the subtitles refer to the deviation of ΔK relative to K_a.



(a) (b)

Figure 2. The effect of using a mismatched filter on imaging results in real-scene SAR echo imaging processing. The deviation of ΔK relative to K_a in (**b**) is 4%.

2.3. ABEW

Considering that the mismatched filter will cause tailing in the azimuth direction, the degree of edge widening in the azimuth direction of SAR images can be used to assess the degree of main lobe widening in that direction, thereby assessing the quality of SAR images. Researchers at the Arizona State University proposed a method of using the edge width of image motion direction as a measure of motion blur [26,27], and this has been widely studied and applied. However, this algorithm is only suitable for assessing the degree of blur under a high signal-to-noise ratio. The SAR system uses microwave signals for imaging, and these signals are coherent in the echo. When the echo signals come from multiple scatterers, they interfere with each other, resulting in speckle noise that reduces the signal-to-noise ratio of the SAR image. Therefore, for SAR images containing coherent speckle, the assessment of defocus blur is not ideal.

The background of SAR images composed of coherent speckle noise has false edges, and its edge width cannot represent the actual degree of edge widening caused by the mismatched filter, which seriously affects the calculation of the edge width. Therefore, it is necessary to remove the background in SAR images and extract the salient area. Gills uses the complexity of local signals in the image to define saliency [28]. The higher the complexity of the local area, the flatter their grayscale histogram distribution, and the higher the information entropy. Therefore, the maximum local information entropy is considered to extract the salient area from SAR images. The information entropy of an image is defined as

$$InEn = -\sum_{n=0}^{2^{\beta}-1} p(n)\log_2 p(n) \tag{15}$$

where n is the grayscale value contained in the image, with a value range of $(0, 2^{\beta}-1)$, β is the bit number of the image, and p is the probability of each grayscale value appearing in the image.

The steps to extract the salient regions of SAR images are as follows:

(1) The size of the input SAR image is [M, N], and the calculation window size is defined as 64 pixels × 64 pixels.
(2) Calculate the information entropy $InEn(x, y)$ within the window at each pixel position of the input image, and calculate the mean information entropy $T = mean(InEn)$.
(3) Count the points in the image where $InEn(x, y) > T$, define this point as the salient point, and calculate the number n of salient points.
(4) If $n > 20\%MN$, then the mean $T = T + 0.1$, and return to step (3). Otherwise, terminate the operation and output the SAR salient area image.

A window that is too small may lead to the excessive consumption of computational resources and time, whereas a window that is too large may result in the blurring of image features, thereby impairing the accurate extraction of salient regions within the image. To balance computational efficiency and feature extraction capability, we set the calculation window size to 64 pixels × 64 pixels. This window size has been experimentally validated

to effectively capture sufficient spatial features and texture information while maintaining computational efficiency.

Blurred edge points (BEPs) are defined as points in the salient area of the image at which the grayscale gradient direction is perpendicular to the azimuth direction. A one-dimensional Sobel operator parallel to the azimuth was used to determine the position of BEPs in the salient area and to further reduce the interference of coherent speckle noise, while selecting strong target points with grayscale values larger than $2^{\beta-8} \cdot 10^2$ as the BEPs. The blurred edge width is defined as the width of a data segment with monotonicity at both ends along the defocus direction starting from the BEP; that is, the pixel interval between the maximum and minimum grayscale pixels with a monotonic relationship along the azimuth direction. As shown in Figure 3, Figure 3a is an SAR image of a real scene Figure 3b is the result obtained by extracting salient area from Figure 3a, indicating that the background area has been removed; and Figure 3c is the result obtained by extracting BEPs from Figure 3b. The azimuth profile of a BEP in Figure 3c is shown in Figure 4, where point B is a BEP extracted from the salient area of the SAR image, and points A and C are the two endpoints of the point B that have a monotonic relationship along the azimuth direction. Therefore, the blurred edge width of point B is the pixel interval between points A and C.

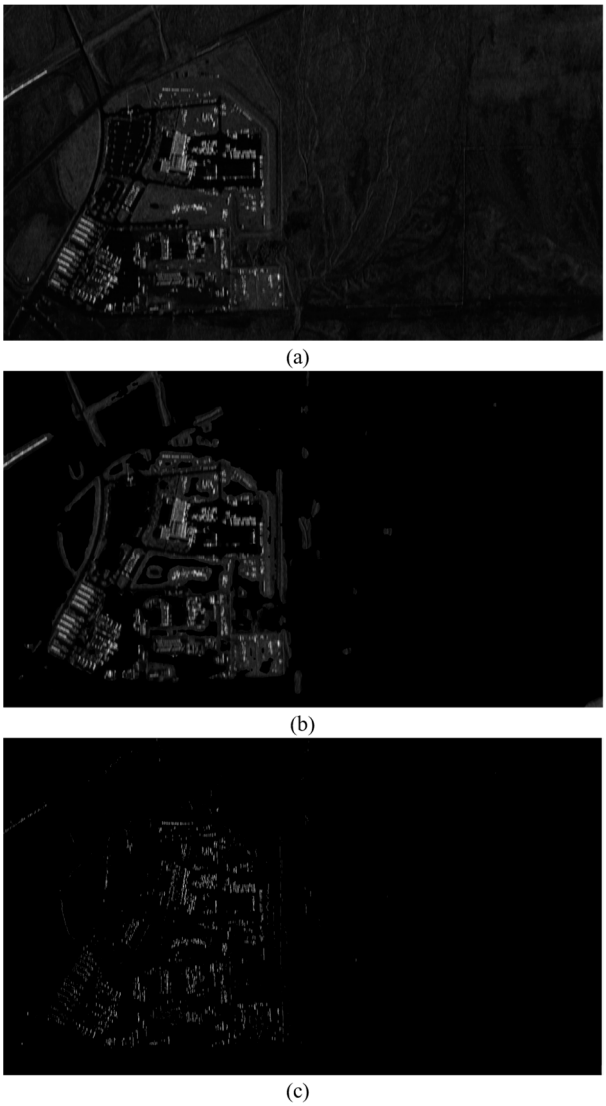


Figure 3. Extracting salient area and BEPs from original SAR image. (**a**) is the real scene SAR image, (**b**) is the result obtained by extracting salient area from (**a**), and (**c**) is the result obtained by extracting BEPs from (**b**).

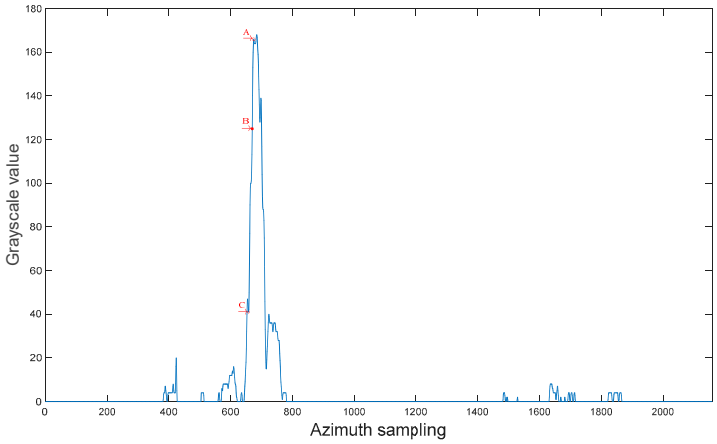


Figure 4. The azimuth profile of a BEP. Point B is a BEP extracted from the salient area of the SAR image, and points A and C are the two endpoints of point B that have a monotonic relationship along the azimuth direction.

ABEW is defined as

$$ABEW = \frac{1}{N}\sum_{i=1}^{N} w_i \tag{16}$$

where N is the number of BEPs in the salient area of SAR images and w_i is the blurred edge width of the BEPs in the azimuth direction.

2.4. Decomposition of Transfer Functions in the Frequency Domain

Because the flight trajectory is not ideal, the echo data are mismatched with the matched filter derived under the ideal flight parameters in Equation (8), resulting in an inability to achieve precise focusing. This therefore needs to be corrected.

Expand the square root in Equation (5) into a power series of f_τ and f_a, and retain it in the fourth order; the phase becomes

$$\begin{aligned}\theta_{2df}(f_\tau, f_a) = -\frac{4\pi R_0 f_c}{c}\Big(\quad & 1 + \frac{f_\tau}{f_c} - \frac{c^2}{8v^2 f_c^2} f_a^2 + \frac{c^2}{8v^2 f_c^3} f_a^2 f_\tau \\ & - \frac{c^4}{128 v^4 f_c^4} f_a^4 - \frac{c^2}{8v^2 f_c^4} f_a^2 f_\tau^2 \Big) - \frac{\pi f_\tau^2}{k_r}\end{aligned} \tag{17}$$

where the first, third, and fifth terms in the brackets are derived from the azimuth modulation, which is a function of the azimuth frequency f_a related to the point target position R_0. They can be approximately regarded as the results of retaining the fourth-order term after the azimuth modulation term in Equation (7) has expanded in the power series. The second and fourth terms in the brackets are derived from RCM, which can be approximately regarded as the result of retaining the second-order term after the RCM term in Equation (7) has been expanded in the power series. The last term in the brackets is derived from the cross-coupling of the range and azimuth, which can be approximately regarded as the result of retaining the first-order term after the cross-coupling term in Equation (7) has been expanded in the power series, and together with the last term in Equation (17), it constitutes the range modulation. From the results analyzed in Section 2.2, it can be seen that the azimuth modulation in the filter predominantly affects the filtering result, and despite a small degree of error, the degradation of the image quality is extremely serious, which is consistent with the larger proportion of the azimuth modulation term in Equation (17). Correspondingly, the phase of the matched filter becomes

$$\begin{aligned}\theta_{MF}(f_\tau, f_a) = \frac{4\pi R_0 f_c}{c}\Big(\quad & - \frac{c^2}{8v^2 f_c^2} f_a^2 + \frac{c^2}{8v^2 f_c^3} f_a^2 f_\tau \\ & - \frac{c^4}{128 v^4 f_c^4} f_a^4 - \frac{c^2}{8v^2 f_c^4} f_a^2 f_\tau^2 \Big) + \frac{\pi f_\tau^2}{k_r}\end{aligned} \tag{18}$$

Since the k_r of the radar transmission signal is known and fixed, the mismatch error of the filter mainly exists in the first four terms in Equation (18). For the convenience of the following analysis, the first four terms are written separately:

$$\varphi(f_\tau, f_a) = -\frac{\pi c R_0}{2v^2 f_c} f_a^2 + \frac{\pi c R_0}{2v^2 f_c^2} f_a^2 f_\tau - \frac{\pi c R_0}{2v^2 f_c^3} f_a^2 f_\tau^2 - \frac{\pi c^3 R_0}{32 v^4 f_c^3} f_a^4 \tag{19}$$

It can be seen from Equation (19) that the coefficients of the filter are composed of radar parameters and flight parameters, so that the error caused by the flight trajectory deviation is reflected in each coefficient. In order to analyze the influence of the errors in each coefficient on the quality of the imaging result, errors of varying degrees are introduced into each coefficient separately, and the trend in the image quality change is observed, as shown in Figure 3.

As can be seen from Figure 5, the coefficient of the f_a^2 term is sensitive to errors, as even a small error will cause a rapid increase in ABEW. Moreover, the f_a^2 term is derived from the azimuth modulation, which is consistent with the results analyzed in Section 2.2, reporting that the accuracy of the azimuth modulation in the filter is the main influence on imaging quality. Figure 5 also shows that the quality of the imaging result is mainly affected by the accuracy of the low-order coefficients. As the order increases, the influence of the coefficient error on the imaging result gradually decreases. Therefore, in order to solve the defocusing of the imaging result caused by the flight trajectory deviations, the IQA index proposed in Section 2.3 can be used to correct the coefficients of each item in Equation (19), according to the degree of influence on the quality of the imaging result.

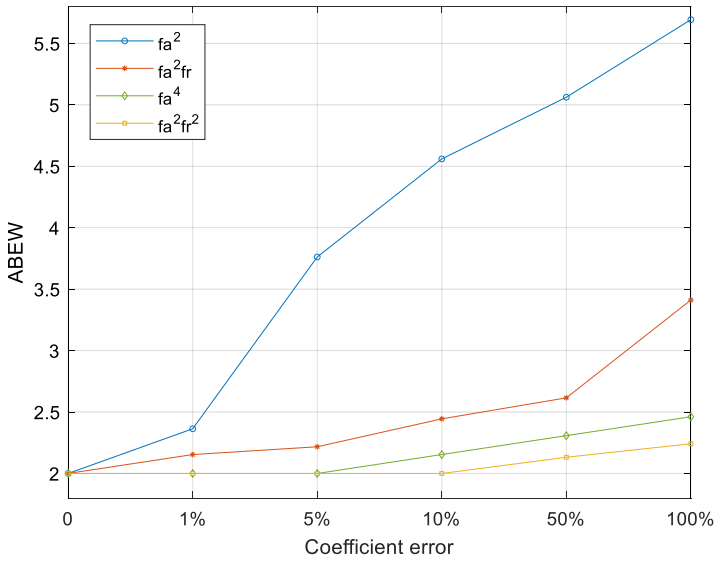


Figure 5. The influence of the errors in each coefficient on the quality of the imaging result.

3. Experimental Results

3.1. SAR IQA Using ABEW

In order to verify the effectiveness of ABEW in SAR IQA, different degrees of frequency modulation rate errors were introduced into real-scene SAR echo data to obtain imaging results with different defocusing degrees. The presented algorithm is validated by more than forty real-scene SAR images, in which the sampling point numbers are 2160 on the azimuth direction and 3840 on the range direction. As shown in Figure 6, from a subjective point of view, as the frequency modulation rate error increases, the quality of SAR images from (a) to (e) shows a significant decrease. The left side of Figure 6 shows the real-scene SAR image, and the right side shows the detailed part of the image. Figure 7 shows the assessment results of the SAR image shown in Figure 6 by the traditional IQA algorithm and the ABEW in the salient area algorithm.

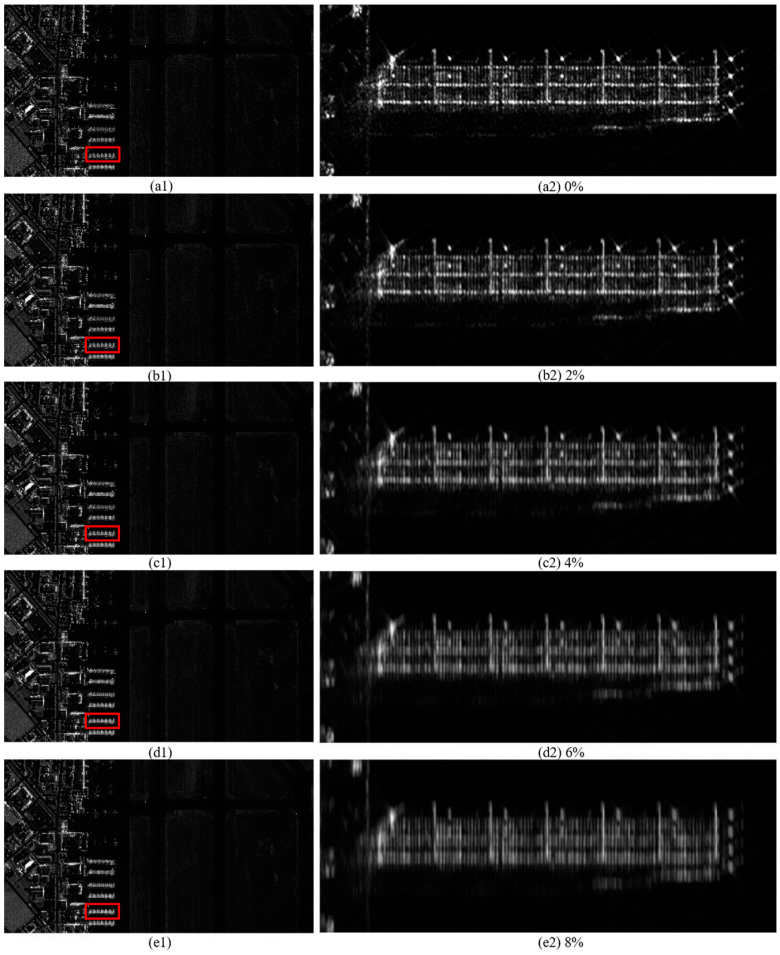


Figure 6. Real-scene SAR images under different frequency modulation rate errors.

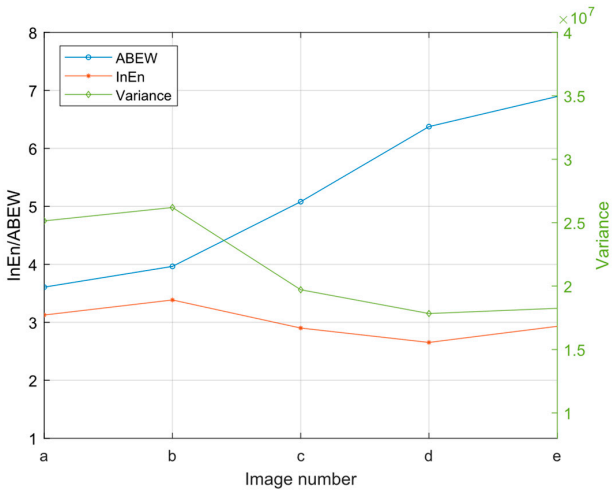


Figure 7. Comparison of InEn, variance, and ABEW.

From Figure 7, it can be seen that as the image quality decreases, the traditional IQA index changes irregularly. For example, the information entropy in Figure 6(e1) is larger than that in Figure 6(d1). Therefore, traditional IQA indexes cannot accurately reflect the quality of the image, while the change in ABEW fully conforms to the change in image quality. As the image quality decreases, the ABEW gradually increases. Through the above experimental analysis, it can be concluded that the ABEW index proposed in this article can effectively assess the quality of SAR images. The smaller the value of the index, the better the image quality.

3.2. Maneuvering Trajectory SAR Processing Using the Decomposition of Transfer Functions in the Frequency Domain

In order to evaluate the correction capability of the matched filter in Equation (18) for the imaging results of echo data in which the flight trajectory is not ideal, the flight altitude and flight speed in the radar parameters are introduced into random fluctuations to simulate the error caused by the trajectory deviation, and the echo data of a single-point target is generated under this condition. The specific parameters are shown in Table 1. The ideal flight parameters are used for the initial values of the coefficients in Equation (19), and ABEW is used as the IQA index. The coefficients are corrected in sequence, starting from the low-order terms.

Table 1. Parameter list.

Parameter	Value
Speed of light (c)	3×10^8 m/s
Wavelength (λ)	0.03125 m
Signal bandwidth (B_r)	200 MHz
Pulse duration (T)	1 us
Pulse repeat frequency (PRF)	1382.4 Hz
Sampling frequency (f_s)	1 GHz
Flight altitude (H) (ideal)	3000 m
Platform velocity (v) (ideal)	300 m/s
Rand velocity error along the altitude direction	$(-1, 1)$ m/s
Rand velocity error along the azimuth direction	$(-10, 10)$ m/s

The correction steps for each coefficient are as follows:

(1) The search range is D, the number of search points is N, the ABEW error accuracy is δ, the number of searches is i, and $i = 1$ is set. The ideal flight parameters are used as the initial value of the coefficient x_0, and the ABEW value of the filtered imaging result at this time is calculated and recorded as val_1.

(2) The current coefficient search range is set to $(x_0 - D/i, x_0 + D/i)$, the coefficient values are divided within the range into $N * i$ parts, the ABEW value of the imaging result is calculated after the echo data have been processed by the filter under the current coefficient, and the minimum value of ABEW and the corresponding coefficient value are found, recorded as val_2 and x_0, respectively.

(3) If $val_2 < val_1$, set $val_1 = val_2$. If $|val_2 - val_1| > \delta$, then $i = i + 1$, and return to step (2); otherwise, terminate the operation and output x_0.

The echo data are processed using the filter whose coefficients are corrected item by item, and the ABEW value of the processing result is shown in Figure 8. From Figure 8, it can be seen that the ABEW value shows a downward trend with the correction of the coefficients item by item, which means that the imaging result is gradually optimized. The comparison of processing results before and after the correction of filter coefficients for single point target SAR echo data is shown in Figure 9, where Figure 9(a1,b1,c1) are the imaging results of the single-point target, the range profile, and the azimuth profile when the ideal flight parameters are used for the filter coefficients, and the peak sidelobe ratios are -13.0285 dB and -0.9516 dB, respectively. Figure 9(a2,b2,c2) are the imaging results of the single-point target, the range profile, and the azimuth profile when the corrected coefficients are used as the filter coefficients, and the peak sidelobe ratios are -13.1227 dB and -12.6601 dB, respectively. As can be seen from Figure 9, the imaging results of the single-point target after the filter coefficients have been corrected are better than before the correction, and the ABEW results and the peak sidelobe ratio values also show corresponding changes. The comparison of processing results before and after the correction of filter coefficients for real-scene SAR echo data is shown in Figure 10, where Figure 10(a1,b1) shows the real-scene SAR image, and Figure 10(a2,b2) shows the detailed part of the image. Figure 10(a1) are the imaging results when the ideal flight parameters are used for the filter coefficients, and the value of ABEW is 10.798. Figure 10(b1) are the imaging results when the

corrected coefficients are used as the filter coefficients, and the value of ABEW is 7.251. As can be seen from Figure 10 and ABEW value, the imaging result after filter coefficient correction is better than before the correction. From the above experiments, it can be demonstrated that, by decomposing the transfer function in the frequency domain and using ABEW as the IQA index to optimize the filter coefficients item by item, the echo data can be processed when the flight trajectory is not ideal, and an ideal imaging result can be obtained.

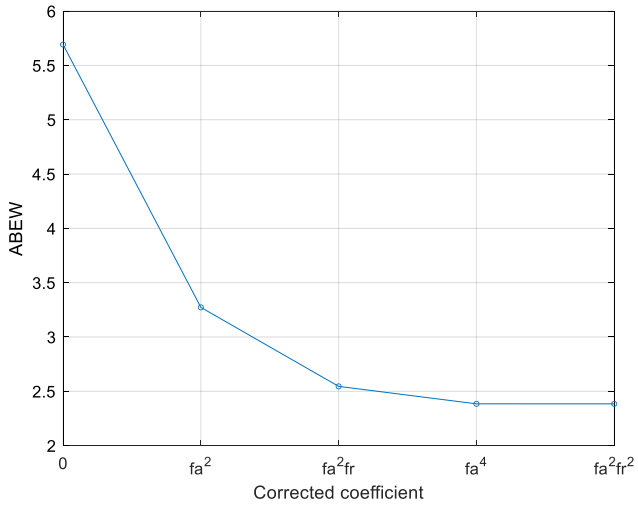


Figure 8. The ABEW value of the processing result when the single-point target SAR echo is processed using a filter with the coefficient correction item by item.

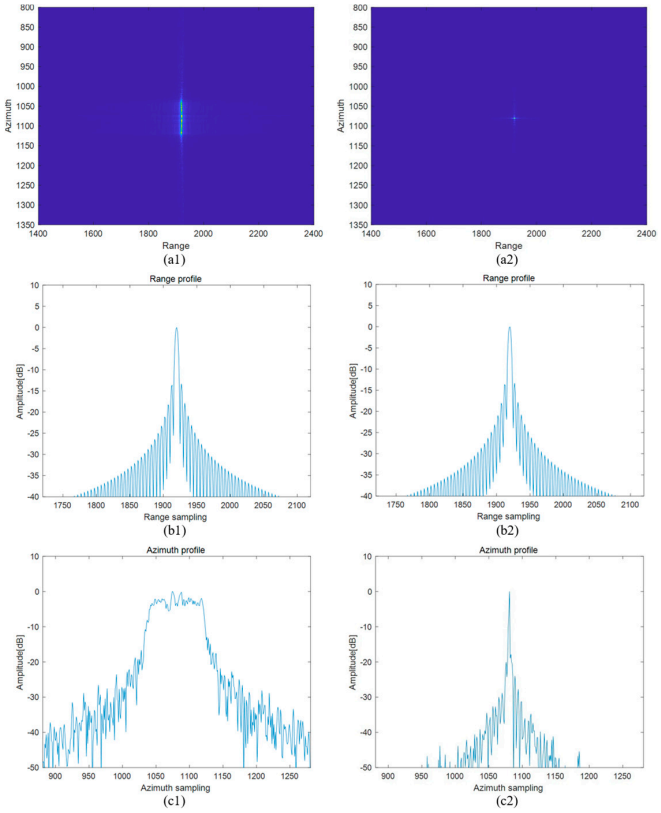


Figure 9. The comparison of the processing results before and after the correction of filter coefficients for single point target SAR echo data. (**a1**–**c1**) are the imaging results of the single-point target, the range profile, and the azimuth profile when the ideal flight parameters are used for the filter coefficients. (**a2**–**c2**) are the imaging results of the single-point target, the range profile, and the azimuth profile when the corrected coefficients are used as the filter coefficients.

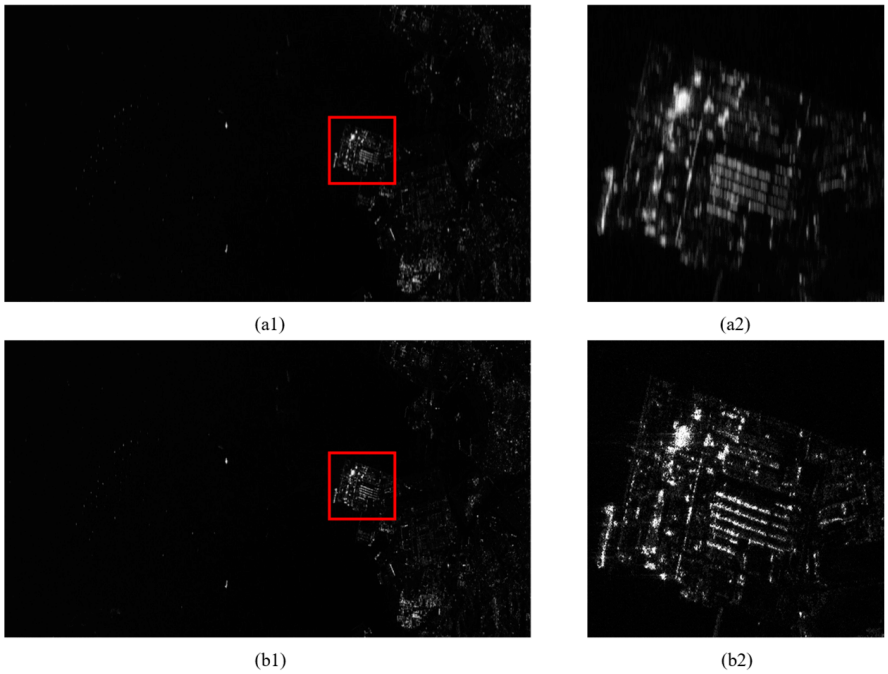


Figure 10. The comparison of the processing results before and after the correction of filter coefficients for real scene SAR echo data. (**a1**,**a2**) are the imaging results when the ideal flight parameters are used for the filter coefficients, and (**b1**,**b2**) are the imaging results when the corrected coefficients are used as the filter coefficients.

4. Conclusions

Based on the principles of SAR imaging, this paper analyzes the impact of defocusing caused by mismatched filters on the imaging results and proposes a non-reference SAR IQA index based on ABEW in the salient area. The presented algorithm and traditional SAR IQA indexes were compared using more than forty real-scene SAR images, and it was found that ABEW can achieve higher consistency with the actual image quality without the original reference image, which provided a new idea and method for the IQA of SAR. In addition, this paper also proposes an idea of decomposing the transfer function in the frequency domain and fitting the matched filter with a polynomial. The estimation of the flight trajectory was changed into a correction of the matched filter, avoiding the precise estimation of Doppler parameters and complex calculation during the time–frequency conversion process. Errors were introduced during the flight to generate an echo signal for testing, and the filter was corrected in conjunction with ABEW. The experimental results show that, compared with the pre-correction, using the corrected matched filter can yield better imaging results, which provides a new idea and method for echo data imaging processing when the flight trajectory is not ideal.

Author Contributions: Conceptualization, C.Y. and K.W.; Data curation, C.Y.; Formal analysis, C.Y.; Funding acquisition, D.W. and K.W.; Investigation, C.Y., D.W. and F.S.; Methodology, C.Y.; Project administration, D.W., F.S. and K.W.; Resources, K.W.; Software, C.Y.; Supervision, D.W. and K.W.; Validation, C.Y. and D.W.; Visualization, C.Y.; Writing—original draft, C.Y.; Writing—review and editing, C.Y. and K.W. All authors have read and agreed to the published version of the manuscript.

Funding: This research received no external funding.

Data Availability Statement: Data are contained within the article.

Conflicts of Interest: The authors declare no conflicts of interest.

Abbreviations

The following abbreviations are used in this manuscript:

SAR	synthetic aperture radar
ABEW	average blurred edge width
IQA	imaging quality assessment
UAV	unmanned aerial vehicle
POSP	principle of stationary phase
GPS	global positioning satellite
IMU	inertial measurement unit
SSIM	structural similarity
TSSIM	texture-based SSIM
RCM	range cell migration
BEPs	blurred edge points

References

1. Moreira, A.; Prats-Iraola, P.; Younis, M.; Krieger, G.; Hajnsek, I.; Papathanassiou, K.P. A tutorial on synthetic aperture radar. *IEEE Geosci. Remote Sens. Mag.* **2013**, *1*, 6–43. [CrossRef]
2. Brusch, S.; Lehner, S.; Fritz, T.; Soccorsi, M.; Soloviev, A.; Van Schie, B. Ship surveillance with TerraSAR-X. *IEEE Trans. Geosci. Remote Sens.* **2010**, *49*, 1092–1103. [CrossRef]
3. Tsokas, A.; Rysz, M.; Pardalos, P.M.; Dipple, K. SAR data applications in earth observation: An overview. *Expert Syst. Appl.* **2022**, *205*, 117342. [CrossRef]
4. Zhu, B.; Yang, C.; Dai, J.; Fan, J.; Qin, Y.; Ye, Y. R 2 FD 2: Fast and Robust Matching of Multimodal Remote Sensing Images via Repeatable Feature Detector and Rotation-invariant Feature Descriptor. *IEEE Trans. Geosci. Remote Sens.* **2023**, *61*, 1–15.
5. Ye, Y.; Zhu, B.; Tang, T.; Yang, C.; Xu, Q.; Zhang, G. A robust multimodal remote sensing image registration method and system using steerable filters with first-and second-order gradients. *ISPRS J. Photogramm. Remote Sens.* **2022**, *188*, 331–350. [CrossRef]
6. Aguasca, A.; Acevo-Herrera, R.; Broquetas, A.; Mallorqui, J.J.; Fabregas, X. ARBRES: Light-weight CW/FM SAR sensors for small UAVs. *Sensors* **2013**, *13*, 3204–3216. [CrossRef] [PubMed]
7. Acevo-Herrera, R.; Aguasca, A.; Mallorquí, J.J.; Fàbregas, X. High-compacted FM-CW SAR for boarding on small UAVs. In Proceedings of the 2009 IEEE International Geoscience and Remote Sensing Symposium, Cape Town, South Africa, 12–17 July 2009; pp. II-543–II-546.
8. Lort, M.; Aguasca, A.; Lopez-Martinez, C.; Marín, T.M. Initial evaluation of SAR capabilities in UAV multicopter platforms. *IEEE J. Sel. Top. Appl. Earth Obs. Remote Sens.* **2017**, *11*, 127–140. [CrossRef]
9. Zhang, L.; Qiao, Z.; Xing, M.-d.; Yang, L.; Bao, Z. A robust motion compensation approach for UAV SAR imagery. *IEEE Trans. Geosci. Remote Sens.* **2012**, *50*, 3202–3218. [CrossRef]
10. Eldhuset, K. A new fourth-order processing algorithm for spaceborne SAR. *IEEE Trans. Aerosp. Electron. Syst.* **1998**, *34*, 824–835. [CrossRef]
11. Eldhuset, K. Ultra high resolution spaceborne SAR processing. *IEEE Trans. Aerosp. Electron. Syst.* **2004**, *40*, 370–378. [CrossRef]
12. Cumming, I.G.; Wong, F.H. Digital processing of synthetic aperture radar data. *Artech House* **2005**, *1*, 108–110.
13. Kennedy, T.A. Strapdown inertial measurement units for motion compensation for synthetic aperture radars. *IEEE Aerosp. Electron. Syst. Mag.* **1988**, *3*, 32–35. [CrossRef] [PubMed]
14. Jun, S.; Long, M.; Xiaoling, Z. Streaming BP for non-linear motion compensation SAR imaging based on GPU. *IEEE J. Sel. Top. Appl. Earth Obs. Remote Sens.* **2013**, *6*, 2035–2050. [CrossRef]
15. Ferretti, A.; Savio, G.; Barzaghi, R.; Borghi, A.; Musazzi, S.; Novali, F.; Prati, C.; Rocca, F. Submillimeter accuracy of InSAR time series: Experimental validation. *IEEE Trans. Geosci. Remote Sens.* **2007**, *45*, 1142–1153. [CrossRef]
16. Bennett, J.R.; Cumming, I.G. A digital processor for the production of SEASAT synthetic aperture radar imagery. In Proceedings of the Symposium on Machine Processing of Remotely Sensed Data, West Lafayette, IN, USA, 27–29 June 1979; Paper 316.
17. Curlander, J.; Wu, C.; Pang, A. Automated preprocessing of spaceborne SAR data. In Proceedings of the 1982 International Geoscience and Remote Sensing Symposium, Munich, Germany, 1–4 June 1982.
18. Carra, W.; Goodman, R.; Majewski, R. *Spotlight Synthetic Aperture Radar-Signal Processing Algorithm*; Artech House: Norwood, MA, USA, 1995.
19. Jakowatz, C.V.; Wahl, D.E.; Eichel, P.H.; Ghiglia, D.C.; Thompson, P.A. *Spotlight-Mode Synthetic Aperture Radar: A Signal Processing Approach: A Signal Processing Approach*; Springer Science & Business Media: New York, NY, USA, 2012.
20. Eldhuset, K. High-resolution spaceborne SAR processing using the decomposed transfer function. *IEEE Trans. Aerosp. Electron. Syst.* **2017**, *53*, 2187–2198. [CrossRef]
21. Nolan, A.R.; Goley, G.S.; Bakich, M. Performance estimation of SAR using NIIRS techniques. In Proceedings of the Algorithms for Synthetic Aperture Radar Imagery XIX, Baltimore, MD, USA, 25–26 April 2012; pp. 248–258.

22. Pestel-Schiller, U.; Ostermann, J. Subjective evaluation of compressed SAR images using JPEG and HEVC intra coding: Sometimes, compression improves usability. In Proceedings of the 2018 15th European Radar Conference (EuRAD), Madrid, Spain, 26–28 September 2018; pp. 154–157.
23. Jiao, S.; Dong, W. SAR image quality assessment based on SSIM using textural feature. In Proceedings of the 2013 Seventh International Conference on Image and Graphics, Qingdao, China, 26–28 July 2013; pp. 281–286.
24. Lu, X.; Sun, H. Parameter assessment for SAR image quality evaluation system. In Proceedings of the 2007 1st Asian and Pacific Conference on Synthetic Aperture Radar, Huangshan, China, 5–9 November 2007; pp. 58–60.
25. Yao, S.; Lei, G.; Ren, Z. Study on missile-borne SAR imaging quality assessment based on global features. In Proceedings of the 2022 2nd International Conference on Computer Graphics, Image and Virtualization (ICCGIV), Chongqing, China, 23–25 September 2022; pp. 124–129.
26. Ferzli, R.; Karam, L.J. A no-reference objective image sharpness metric based on the notion of just noticeable blur (JNB). *IEEE Trans. Image Process.* **2009**, *18*, 717–728. [CrossRef] [PubMed]
27. Narvekar, N.D.; Karam, L.J. A no-reference image blur metric based on the cumulative probability of blur detection (CPBD). *IEEE Trans. Image Process.* **2011**, *20*, 2678–2683. [CrossRef] [PubMed]
28. Gilles, S. Robust Description and Matching of Images. Ph.D. Thesis, Department of Engineering Science, University of Oxford, Oxford, UK, 1998.

Disclaimer/Publisher's Note: The statements, opinions and data contained in all publications are solely those of the individual author(s) and contributor(s) and not of MDPI and/or the editor(s). MDPI and/or the editor(s) disclaim responsibility for any injury to people or property resulting from any ideas, methods, instructions or products referred to in the content.